
Article:
Chen, X., Wang, J. orcid.org/0000-0003-4870-3744, Patel, V.I. et al. (1 more author) (2016) A Nine-Phase 18-Slot 14-Pole Interior Permanent Magnet Machine with Low Space Harmonics for Electric Vehicle Applications. IEEE Transactions on Energy Conversion, 31 (3). pp. 860-871. ISSN 0885-8969

https://doi.org/10.1109/TEC.2016.2538321

A Nine-Phase 18-Slot 14-Pole Interior Permanent Magnet Machine with Low Space Harmonics for Electric Vehicle Applications

Xiao Chen, Member, IEEE, Jiabin Wang, Senior Member, IEEE, Vipulkumar I. Patel, Member, IEEE and Panagiotis Lazari, Student Member, IEEE

Abstract--One of the key challenges of utilizing concentrated winding in Interior Permanent-magnet Machines (IPMs) is the high rotor eddy-current losses in both magnets and rotor iron due to the presence of a large number of lower and higher order space harmonics in the stator Magneto-Motive Force (MMF). These MMF harmonics also result in other undesirable effects, such as localized core saturation, acoustic noise and vibrations. This paper proposes a 9-phase 18-slot 14-pole IPM machine using the multiple 3-phase winding sets to reduce MMF harmonics. All the sub-harmonics and some of the higher order harmonics are cancelled out while the advantages of the concentrate windings are retained. The proposed machine exhibits a high efficiency over wide torque and speed ranges. A 10kW machine prototype is built and tested in generator mode for the experimental validation. The experimental results indicate the effectiveness of the MMF harmonics cancellation in the proposed machine.

Index Terms--MMF space harmonics, multi-phase machine, interior permanent-magnet machine, global optimization, multiple 3-phase winding.

I. Introduction

PERMANENT-Magnet Synchronous Machines (PMSMs) exhibit high torque density and high energy efficiency over a wide operation range, which are preferable attributes for Electric Vehicle (EV) applications [1].

In PMSMs, Surface-mounted Permanent-magnet Machines (SPMs) produce electromagnetic torque purely from the interaction of the permanent-magnet field with armature currents [2, 3]. Without flux focusing effect in SPMs, rare-earth permanent-magnets with a high remanence (such as sintered NdFeB) are usually employed to improve torque density and this often results in relatively more magnet material usage. However, the limited reserves and high cost of the rare-earth materials restrict the potential of PM machine topologies, such as SPMs, which uses more rare-earth magnets, in EV traction applications [4-6]. Further, the conflicting requirements for high torque at low speeds and low back Electro-Motive Force (EMF) at high speeds in EV tractions are very difficult to meet without increase in inverter VA rating.

In contrast, Interior Permanent-magnet Machines (IPMs) with low cost magnet material (such as ferrite and bonded NdFeB) provide more flexibility to strike a good balance between performance and cost, due to both the reluctance torque contribution and flux focusing effect [7, 8]. Hence, IPMs, including Permanent-magnet Assisted Synchronous Reluctance Machines (PMA-SynRMs) proposed in recent years, present a promising solution for EV traction applications [9-11].

Compared to the conventional distributed winding configurations, the advantages of the fractional-slot non-overlapping (concentrated) winding configurations include the high copper packing factor (slot fill factor) particularly with segmented stator structure, short end-winding length, low cogging torque, good field weakening capability due to relatively large d-axis inductance, and good fault tolerant capability owing to low mutual inductance [12]. However, one of the key challenges of utilizing concentrated winding in IPMs is the high rotor eddy-current losses in both magnets and rotor iron due to the presence of a large number of lower and higher order space harmonics in the stator Magneto-Motive Force (MMF) [13, 14]. These MMF harmonics also result in other undesirable effects, such as acoustic noise and vibrations, and the localized core saturation that tend to reduce reluctance torque.

In literature, a number of methods have been proposed to cancel or reduce MMF harmonics, such as employing non-uniform tooth width, using asymmetric number of turns, and applying phase shift by doubling slot numbers [15-17]. The first two methods compromise the machine performance and the third technique no longer has the manufacture advantage of concentrated windings. A delta-star connection is utilized to reduce MMF harmonics by shifting the current phase angle in the delta and star connected windings in [18]. However, the shift angle is restricted to 30°, 150° and 270°, due to the phase angle limits of the delta-star connection, and hence it compromises the MMF harmonic cancellation effect. Moreover, this technique yields a very low winding factor for the working harmonic. Special magnetic flux barriers in stator yoke are introduced in [19] to reduce flux density sub-harmonics in air-gap by changing the magnetic reluctance in

X. Chen, J. Wang and P. Lazari are all with the department of Electronic and Electrical Engineering, The University of Sheffield, Sheffield, S1 3JD, UK (e-mail: x.chen.1988@ieee.org, j.b.wang@sheffield.ac.uk, panos.lazari@sheffield.ac.uk).

V. I. Patel is with Mitsubishi Hitachi Power Systems Europe Ltd., London, W1K 6WE, UK (email: v.i.patel@ieee.org).

specific stator core location. Nevertheless, the mechanical stiffness of the stator is reduced significantly with presence of the flux barriers. This will result in a lower stator natural frequency and increase the risk of resonance within a speed operating range. Multiple 3-phase sets with an appropriate phase shift between them have also been devised to cancel out the undesirable MMF harmonics [20, 21]. However, this approach leads to an overlapping winding configuration, compromising advantages of the concentrated windings.

To reduce the undesirable MMF harmonics while retain the advantages of the concentrated windings, this paper proposes a 9-phase 18-slot 14-pole IPM machine using the multiple 3-phase winding sets.

II. MMF Expressions of Conventional and Multiple 3-phase Winding Configurations

This section will describe the principle of how a multiple 3-phase winding configuration is employed to reduce MMF harmonics. Firstly, generic harmonic-based MMF expressions are analytically derived for any 3-phase fractional-slot concentrated winding with any feasible slot-pole combination. Their MMF harmonics contents are summarized. Thereafter, a multiple 3-phase winding configuration is introduced to provide a new "degree of freedom" in MMF harmonic cancellation mechanism and this lays down a foundation for developing suitable winding configurations with lower MMF space harmonic contents.

A. Generic Harmonic-based MMF Expressions of Conventional 3-Phase Windings

Assuming ABC windings are symmetric and have the same number of turns, the MMF distribution of each phase due to unit current, known as the winding function, can be expressed as Fourier series given in (1).

$$\begin{aligned} n_A(\theta_m) &= \sum_h \left[N_h \cos\left(h\theta_m + \beta_h\right)\right] \\ n_B(\theta_m) &= \sum_h \left[N_h \cos\left(h\theta_m + \beta_h - h\theta_{phm}\right)\right] \\ n_C(\theta_m) &= \sum_h \left[N_h \cos\left(h\theta_m + \beta_h + h\theta_{phm}\right)\right] \end{aligned} \tag{1}$$

where h denotes the harmonic order, N_h is the magnitude of the h^{th} order harmonic, β_h is the phase angle of the h^{th} order harmonic of phase A, θ_{phm} is the mechanical angular displacement between two adjacent phases of a 3-phase winding, and θ_m denotes the space angle at a point of interest in the air-gap with respect to phase A axis as shown in Fig. 1.

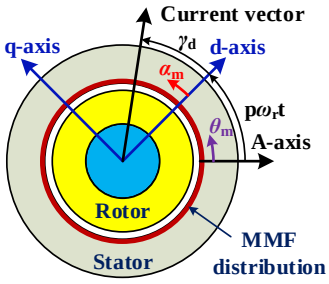

Fig. 1. Current vector diagram in dq0 and ABC coordinate systems.

Due to the symmetrical distribution of a 3-phase winding, θ_{phm}=120° or -120°, depending on the direction of rotation of the MMF working harmonic.

Assuming the current amplitudes in all the phases are identical, the phase currents are expressed by (2).

$$\begin{aligned} i_A &= I\cos\left(p\omega_r t + \gamma_d\right) \\ i_B &= I\cos\left(p\omega_r t + \gamma_d - 120°\right) \\ i_C &= I\cos\left(p\omega_r t + \gamma_d + 120°\right) \end{aligned} \tag{2}$$

where I is the current amplitude, p is the pole pair number, ω_r is the rotor angular speed, t is the time, and γ_d is the phase angle between the current vector and the rotor d-axis as shown in Fig. 1.

The combined MMF of all the 3 phase windings is given in (3).

$$F_s = n_A i_A + n_B i_B + n_C i_C \tag{3}$$

Substituting (1) and (2) into (3), the forward and backward rotating MMF harmonics can be derived and given in (4) and (5) respectively.

$$\begin{aligned} F_f = \frac{1}{2}\sum_h \{ & N_h I[1+2\cos(h\theta_{phm}-120°)] \\ & \cdot\cos[h\alpha_m + (h-p)\omega_r t - \gamma_d + \beta_h]\} \end{aligned} \tag{4}$$

$$\begin{aligned} F_b = \frac{1}{2}\sum_h \{ & N_h I[1+2\cos(h\theta_{phm}+120°)] \\ & \cdot\cos[h\alpha_m + (h+p)\omega_r t + \gamma_d + \beta_h]\} \end{aligned} \tag{5}$$

where $\alpha_m=\theta_m-\omega_r t$.

For a machine with Q slots and p pole pairs, its periodicity r is subject to the greatest common divider between Q and p, as described in (6).

$$r = \mathrm{GCD}\{Q, p\} \tag{6}$$

The orders of harmonics with non-zero magnitudes for the single phase winding function in (1) are summarized in Table I. By way of example, in a double layer winding with the even Q/r, the orders of harmonics with non-zero magnitudes for the single phase winding function are odd numbers 2(h-1)r except jQ, j∈**Z**, where **Z** denotes the positive integer set. This is because the even Q/r can form a symmetric pattern with opposite phasors that are π radians out of phase [22]. The integer multiples of the slot number, jQ, are the numbers of harmonic orders which are cancelled out by the mechanical periodicity. Thereafter, for a 3-phase configuration, windings are uniformly displaced in space with respect to each other by 120° electrical degrees. Therefore, all triplen MMF harmonics of the 3-phase windings are eliminated in Q/r slots. This can also be observed in (4) and (5), where the terms [1+2cos($h\theta_{phm}$-120°)] and [1+2cos($h\theta_{phm}$+120°)] are derived from the 3-phase configuration. Given that jQ is a subset of 3jr, the orders of MMF harmonics with non-zero magnitudes for a double layer 3-phase winding with an even Q/r are odd numbers 2(h-1)r except 3jr. The harmonic order numbers in the other scenarios in Table I can also be derived in the same way.

Compared to conventional distributed windings, the periodicity r in factional-slot concentrated windings is relatively small. Therefore, the latter exhibits more low-order MMF harmonics than the former. To reduce the MMF

harmonics in concentrated windings, a new "degree of freedom" in the MMF harmonic cancellation mechanism will be introduced in the following section.

TABLE I
THE ORDERS OF HARMONICS WITH NON-ZERO MAGNITUDES

Winding type	Double layer winding		
Condition	Q/r is even		Q/r is odd
Non-zero harmonic orders for winding function	(2h-1)r except jQ, j∈**Z**		hr except jQ, j∈**Z**
Non-zero harmonic orders for 3-phase MMF	(2h-1)r except 3jr, j∈**Z**		hr except 3jr, j∈**Z**
Winding type	Single layer winding		
Condition	Q/(2r) is even	Q/(2r) is odd	Q/r is odd & r is even
Non-zero harmonic orders for winding function	(2h-1)r except jQ, j∈**Z**	hr except jQ, j∈**Z**	hr/2 except jQ, j∈**Z**
Non-zero harmonic orders for 3-phase MMF	(2h-1)r except 3jr, j∈**Z**	hr except 3jr, j∈**Z**	hr/2 except 3jr/2, j∈**Z**

B. Generic Harmonic-based MMF Expressions of Multiple 3-Phase Windings

As shown in (4) and (5), the forward and backward MMFs of a conventional 3-phase winding are travelling waves, and the terms [1+2cos($h\theta_{phm}$-120°)] and [1+2cos($h\theta_{phm}$+120°)] lead to the cancellation of all triplen MMF harmonics. To eliminate more MMF harmonics, this paper employs a multiple 3-phase winding configuration to introduce an additional "degree of freedom" in the MMF harmonic cancellation mechanism. This section will derive the generic expressions of the MMF in a multiple 3-phase winding.

Firstly, assuming all 3-phase windings are symmetric and have the same number of turns, the generic MMF distribution of a phase winding in the k^{th} 3-phase set due to unit current, known as the winding function, can be expressed as a Fourier series given in (7) [23].

$$n_k(\theta_m) = \sum_h \left[N_h \cos\left(h\theta_m + \beta_{kh}\right)\right] \tag{7}$$

where k denotes the k^{th} 3-phase set, β_{kh} is the phase angle of the h^{th} order spatial harmonic of the k^{th} set 3-phase winding.

Therefore, the winding functions of each phase (Ak, Bk and Ck) of the k^{th} 3-phase set can be written as (8).

$$\begin{aligned} n_{Ak} &= n_k(\theta_m) \\ n_{Bk} &= n_k\left(\theta_m - \theta_{phm}\right) \\ n_{Ck} &= n_k\left(\theta_m + \theta_{phm}\right) \end{aligned} \tag{8}$$

Assuming the current amplitudes in all the phases are identical, the phase currents of the k^{th} 3-phase set are expressed by (9).

$$\begin{aligned} i_{Ak} &= I\cos\left[p\omega_r t + \gamma_d - (k-1)\theta_\Delta \right] \\ i_{Bk} &= I\cos\left[p\omega_r t + \gamma_d - (k-1)\theta_\Delta - 120^\circ \right] \\ i_{Ck} &= I\cos\left[p\omega_r t + \gamma_d - (k-1)\theta_\Delta + 120^\circ \right] \end{aligned} \tag{9}$$

where θ_Δ is the phase shift angle of the currents between the $(k+1)^{th}$ and k^{th} 3-phase sets.

The combined MMF distribution of multiple 3-phase windings is given in (10).

$$F_s = \sum_k \left(n_{Ak} i_{Ak} + n_{Bk} i_{Bk} + n_{Ck} i_{Ck} \right) \tag{10}$$

Substituting (8) and (9) into (10), the forward and backward MMF equations can be derived and given in (11) and (12) respectively.

$$\begin{aligned} F_f = \frac{1}{2}\sum_h \{ & N_h I[1+2\cos(h\theta_{phm} - 120^\circ)] \\ & \cdot \sum_k \cos[h\alpha_m + (h-p)\omega_r t - \gamma_d + \beta_{kh} + (k-1)\theta_\Delta]\} \end{aligned} \tag{11}$$

$$\begin{aligned} F_b = \frac{1}{2}\sum_h \{ & N_h I[1+2\cos(h\theta_{phm} + 120^\circ)] \\ & \cdot \sum_k \cos[h\alpha_m + (h+p)\omega_r t + \gamma_d + \beta_{kh} - (k-1)\theta_\Delta]\} \end{aligned} \tag{12}$$

where $\alpha_m = \theta_m - \omega_r t$.

Assuming that the currents in each 3-phase set are independently controlled, the h^{th} order MMF harmonic can be cancelled out, if the combined phase shift angles between the k^{th} and $(k+1)^{th}$ 3-phase sets denoted as θ_{fw} and θ_{bw} for the forward and backward MMF harmonics satisfy (13) and (14), respectively.

$$\theta_{fw} = \beta_{(k+1)h} - \beta_{kh} + \theta_\Delta = \pm 360^\circ / K + q_f\, 360^\circ, q_f \in Z \tag{13}$$

$$\theta_{bw} = \beta_{(k+1)h} - \beta_{kh} - \theta_\Delta = \pm 360^\circ / K + q_b 360^\circ, q_b \in Z \tag{14}$$

where K is the number of 3-phase sets. The above conditions lead to the second summation in (11) and (12) becoming zero and hence the h^{th} order harmonic is eliminated. Thus the condition which satisfies (13) and (14) is a new "degree of freedom" in the MMF harmonic cancellation mechanism. It should be noted that realization of the conditions in (13) and (14) requires appropriate phase shifts between two neighboring 3-phase sets in both space and time, denoted by $\beta_{(k+1)h}$-β_{kh} and θ_Δ, respectively.

The selection of K (the number of 3-phase sets) should follow the principle that the single phase winding function N_h only contains even or order harmonics. Therefore, it is recommended that the number of slots per phase should be even numbers.

III. PROPOSED WINDING CONFIGURATION

Based on the foregoing multiple 3-phase winding technique, a 9-phase 18-slot 14-pole winding configuration (three 3-phase sets) is developed in this section. The 9-phase, 18-slot instead of 6-phase or 18-phase is employed such that the number of slots per phase is 2 in a 9-phase configuration and thereby the single phase winding function N_h only contains odd order harmonics. In this way, minimal MMF harmonic contents can be reached.

The MMF harmonic cancellation principle can also be illustrated by the schematic of the resultant MMF vectors shown in Fig. 2. In Fig. 2 (a), three 3-phase winding sets, viz., phases ABC, DEF and GHI, are uniformly distributed in space but with a specific spatial phase angle with respect to each other. To cancel out a given order MMF harmonic, an appropriate space and time phase shifts need to be selected in order to ensure that the MMF vectors of phases ABC, DEF and GHI at this order form a balanced 3-phase system, as illustrated in Fig. 2 (c). However, to maximize the fundamental winding factor, the working harmonics of the MMF vectors of phases ABC, DEF and GHI should be ideally in-phase, as

shown in Fig. 2 (b).

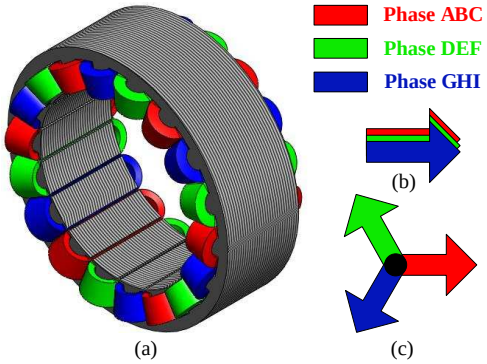

Fig. 2. Schematics for the proposed 9-phase 18-slot 14-pole winding configuration. (a). Winding arrangement. (b). MMF vectors for the working harmonic. (c). MMF vectors for some unwanted harmonics.

-260° phase shift in space and 20° phase shift in time are selected in the proposed 9-phase 18-slot 14-pole winding configuration. The selection of space and time phase shifts will be described later. Fig. 3 depicts the detailed winding arrangements of the conventional 3-phase and the proposed 9-phase 18-slot 14-pole windings.

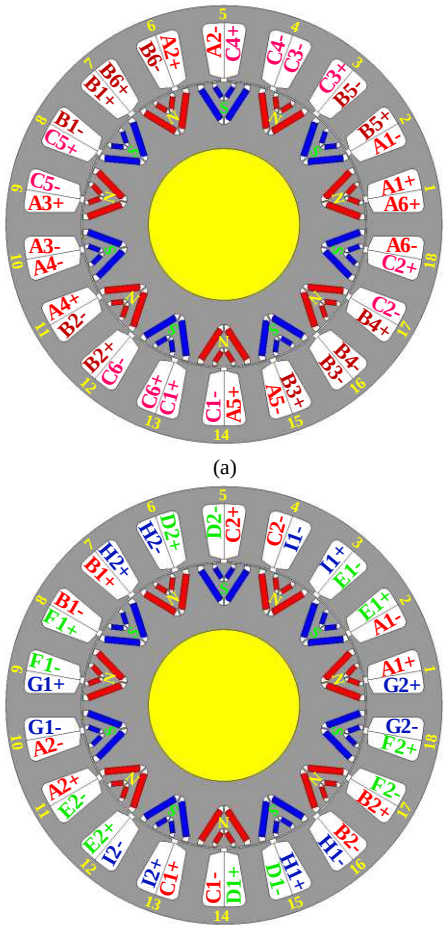

Fig. 3. Schematics of the conventional 3-phase and the proposed 9-phase 18-slot 14-pole winding configurations. (a) 3-phase. (b) 9-phase.

To demonstrate the MMF harmonic cancellation effects in the proposed 9-phase 18-slot 14-pole winding configuration, Table II lists the spatial shift angle $\beta_{(k+1)h}$-β_{kh} for MMF harmonic orders up to 29. The spatial shift of the 1st order MMF harmonic is -260° because phase D is 13 slots lagging phase A and each slot occupies 20° mechanical degrees in space, as shown in Fig. 3 (b). When the current phase shift angle θ_Δ is selected to be 20°, the combined MMF harmonic phase shift angle θ_{fw}= $\beta_{(k+1)h}$-β_{kh}+θ_Δ becomes -240° (or 120°), and satisfies (13). Hence the 1st order forward rotating harmonic is eliminated. It should be noted that the 1st order backward rotating harmonic does not exist in the machine, and this is denoted by "×" in Table II. Similarly, the combined phase shift angles θ_{fw} and θ_{bw} of the 5th, 13th, 17th, 19th, 23rd ⋯ order MMF harmonics satisfy (13) and (14), and therefore they are cancelled out.

The reduction in MMF harmonics can also be observed in the MMF spectra of the 3-phase and 9-phase winding configurations shown in Fig. 4. By employing the proposed winding configuration, the 1st, 5th, 13th, 17th, 19th, 23rd ⋯ order harmonics are cancelled out while the 7th (working harmonic for 14-pole), 11th, 25th, 29th ⋯ order harmonics slightly increase. The slight increases in the 7th, 11th, 25th, 29th ⋯ order harmonics are due to the fact that the 9-phase winding configuration has less number of coils per phase and hence higher winding distribution factor for each harmonic compared to the 3-phase counterpart.

TABLE II
CANCELLATION OF FORWARD AND BACKWARD MMF HARMONICS FOR 18-SLOT 14-POLE 9-PHASE WINDING CONFIGURATION

Harmonic order h	Shift spatial angle $\beta_{(k+1)h}$-β_{kh}	Forward phase angle θ_{fw}=$\beta_{(k+1)h}$-β_{kh}+θ_Δ	Backward phase angle θ_{bw}=$\beta_{(k+1)h}$-β_{kh}-θ_Δ
1	-260° (or 100°)	120°	×
5	-1300° (or 140°)	×	120°
7	-1820° (or 340°)	0°	×
11	-2860° (or 20°)	×	0°
13	-3380° (or 220°)	240°	×
17	-4420° (or 260°)	×	240°
19	-4940° (or 100°)	120°	×
23	-5980° (or 140°)	×	120°
25	-6500° (or 340°)	0°	×
29	-7540° (or 20°)	×	0°

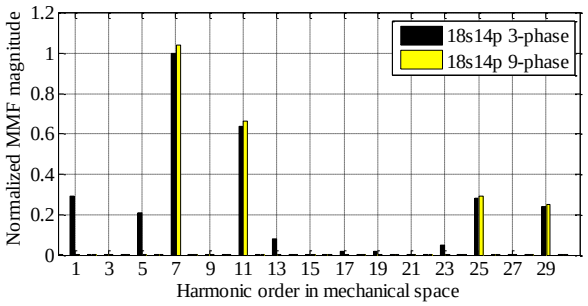

Fig. 4. Comparison of normalized MMF spectra of 3-phase and 9-phase 18-slot 14-pole winding configurations.

IV. MACHINE DESIGN AND GLOBAL OPTIMIZATION

On the basis of the proposed multiple 3-phase winding configuration, a new 9-phase 18-slot 14-pole IPM machine is designed and optimized. The design specifications and constraints are listed in Table III. The optimization objective is to maximize the New European Drive Cycle (NEDC)

efficiency over 12 representative working points as proposed in [24]. Design optimization against any other representative driving cycle can be performed in a similar manner. The optimization constraints include performance specifications, current limit, thermal limit, DC-link voltage (Line-to-line voltage) limit and the limit on the no-load back-EMF at the maximum speed for safety in the event of inverter or control failures, as listed in Table III.

TABLE III
DESIGN SPECIFICATION AND OPTIMIZATION PROCESS

Quantity	Unit	Value
Peak power	kW	10
Rated continuous power	kW	5.0
Base speed	r/min	1350
Maximum speed	r/min	4500
Peak torque at base speed	Nm	70
Rated torque at base speed	Nm	35
Peak torque at maximum speed	Nm	21.0
Continuous torque at maximum speed	Nm	10.5
Current limit	A	22
DC-link voltage(Line-to-line voltage limit)	V	320
No-load line-to-line back-EMF limit	V	600
Cooling		Air-cooled

The optimization is performed using a FE based global optimization package described in [25]. A parameterized FE model is constructed and it is called by the optimization process which evaluates the objective functions and constraints, and selects the most promising designs via a combination of genetic algorithm (GA) and sequential surrogate programming technique.

The leading design parameters to be optimized are shown in Fig. 5. Seven parameters including split ratio, pole arc, pole depth ratio, magnet thickness, tooth width, back-iron thickness and the number of turns per coil, will be optimized. The split ratio K_s is defined as the ratio of the rotor outer radius R_i to the stator outer radius R_o. The pole arc β_p is defined in electrical degree, and hence $\beta_p=p\cdot\beta_p$ where p is the pole pair number. The pole depth ratio K_p is defined as the pole depth D_p divided by the rotor outer radius R_i, as indicated in Fig. 5. Bonded NdFeB magnets with remanence B_r=0.56 and relative recoil permeability μ_r=1.1 are employed for the proposed machine. A representative thermal model is incorporated in the design process to evaluate temperature rise and thermal limit. Similarly, an analytical model is established to adjust the width of the magnet retention bridges so that the maximum stress in the bridges is below the material yield strength at 6750 r/min (1.5 times of the maximum speed).

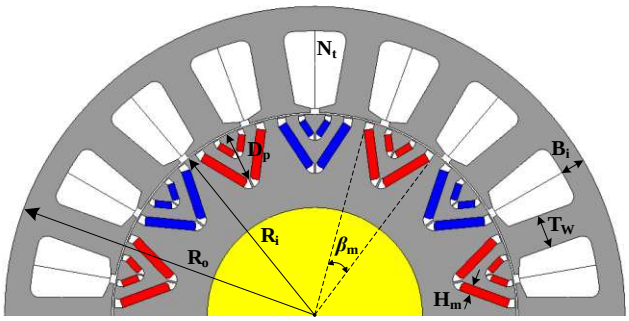

Fig. 5. Geometry parameters illustration

A global optimum is reached after three generations of GA iterations. The total number of designs evaluated in the optimization is 283 and it took 70 hours to complete on a typical PC.

V. PERFORMANCE EVALUATION

A. Performances of the Proposed Machine

The optimization results are listed in Table IV for the machine with outer diameter of 200mm and active length of 66.4mm. The phase back-EMF waveforms at the maximum speed are illustrated in Fig. 6. It can be seen that the phase shift angle between phase D and phase A is 20°, which coincides with the θ_Δ in (9).

TABLE IV
OPTIMIZED PARAMETERS

Quantity	Symbol	Unit	Value
Split ratio	K_s		0.7
Pole arc	β_p	°	162.6
Pole depth ratio	K_p		0.2565
Magnet thickness	H_m	mm	3.875
Tooth width	T_w	mm	15.26
Back-iron thickness	B_i	mm	8.75
NO. of turns per coil	N_t		51

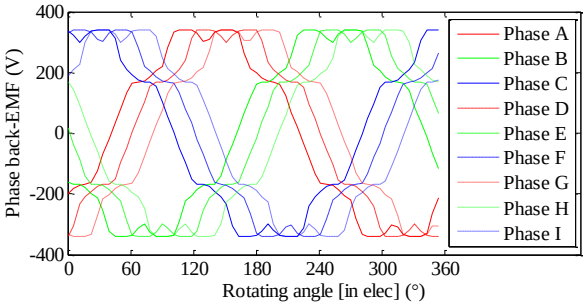

Fig. 6. FE-predicted phase back-EMF waveforms at maximum speed.

The electromagnetic performances at the rated and peak torque at the base speed and over the NEDC driving cycle are shown in Table V. The FE-predicted efficiency map over the toque and speed envelopes is depicted in Fig. 7. It is shown that the proposed machine exhibits high efficiency over wide torque and speed ranges.

TABLE V
PERFORMANCES OF THE PROPOSED MACHINE

Quantity	Unit	Value
Rated current	A	11.1
Rated current density	A/mm^2	7.9
Efficiency at rated torque and base speed	%	93.5%
Peak current	A	22.4
Peak torque ripple	%	5.7%
Efficiency at peak torque and base speed	%	89.1%
Peak line-line voltage	V	326
Max no-load line-line back-EMF	V	564
NEDC efficiency	%	94.2%

The machine performances in field weakening region are also evaluated. By way of example, at 10.5Nm (continuous torque at maximum speed) and 4500r/min, the electromagnetic performances are listed in Table VI. The d- and q-axis current references are determined by Newton-Raphson method to

satisfy both the torque demand and voltage constraint when space vector PWM modulation is employed. It can be observed that the machine efficiency can still reach >94%, demonstrating high efficiency in the field weakening operation.

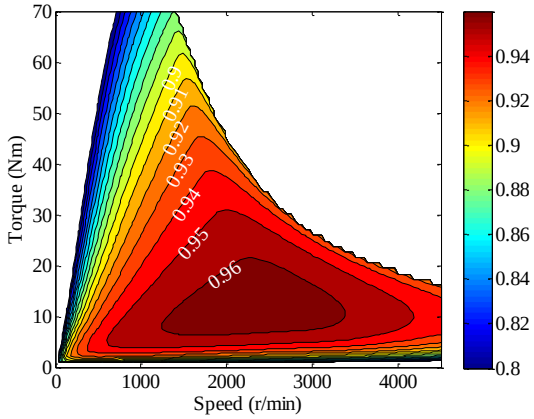

Fig. 7. FE-predicted efficiency map.

TABLE VI
PERFORMANCES AT 10.5NM AND 4500R/MIN

Quantity	Unit	Value
Current amplitude	A	6.2
Copper loss	W	86.4
Rotor iron loss	W	77.7
Stator iron loss	W	135.8
Efficiency	%	94.1%
Torque ripple with respect to peak torque	%	1.7%

B. Performance Comparison with the Conventional 3-Phase Machine

Table VII shows the performance comparison between the conventional 3-phase and the proposed 9-phase 18-slot 14-pole machines. The latter exhibits lower losses and thereby higher efficiency than the former at all the operation conditions (peak, rated and NEDC driving cycle).

By way of example, at peak torque and base speed operation, by using the proposed 9-phase winding configuration, the copper loss, stator iron loss and rotor iron loss are reduced by 11.7%, 2.6% and 10.9% respectively. Therefore, the efficiency is improved by 1.2% (increase from 87.9% to 89.1%).

TABLE VII
PERFORMANCE COMPARISON BETWEEN THE CONVENTIONAL 3-PHASE AND PROPOSED 9-PHASE 18-SLOT 14-POLE MACHINES

Operation condition	Quantity	Unit	3-phase	9-phase
Peak torque and base speed	Copper loss	W	1258.3	1111.5
	Stator iron loss	W	70.0	68.2
	Rotor iron loss	W	28.5	25.4
	Efficiency	%	87.9%	89.1%
	Torque ripple	%	11.5%	5.7%
Rated torque and base speed	Copper loss	W	304.7	274.5
	Stator iron loss	W	48.4	47.7
	Rotor iron loss	W	20.9	19.7
	Efficiency	%	92.9%	93.5%
	Torque ripple	%	7.3%	2.8%
NEDC driving cycle	Copper loss	J	2.7×10^4	2.6×10^4
	Stator iron loss	J	3.0×10^4	2.9×10^4
	Rotor iron loss	J	1.2×10^4	1.1×10^4
	Cycle efficiency	%	93.9%	94.2%

The copper loss reduction is contributed by the winding factor improvement in the proposed 9-phase winding configuration.

The rotor iron loss reduction is attributed to the MMF reduction shown in Fig. 4. Fig. 8 illustrates the harmonic distributions of the rotor iron loss associated with eddy current component for these two machines. It can be observed that the 6^{th}, 12^{th}, 24^{th}, 30^{th}, 42^{nd}, 48^{th}, 60^{th}, 66^{th}, 78^{th} $\cdots$ orders of harmonics in the eddy current loss component of the rotor iron loss are eliminated by using the proposed 9-phase winding configuration. These harmonic orders can be associated with the MMF harmonic orders shown in Fig. 4. By way of example, the 6^{th} order harmonic in the rotor eddy current loss is contributed by the 1^{st} and 13^{th} order harmonics in the stator MMF.

From Fig. 8, it can also be seen that the eddy current loss component in the rotor iron loss associated with the 18^{th} order harmonic is reduced in the proposed machine. This is because for the same torque demand, the proposed machine requires less current amplitude due to the improved winding factor. However, the eddy current loss components associated with the 36^{th}, 54^{th}, 72^{nd}, $\cdots$ orders of harmonics are slightly increased. The increases are attributed to a number of factors. First, the stator MMF harmonics of the orders $(36\pm7)^{th}$, $(54\pm7)^{th}$, $(72\pm7)^{th}$, $\cdots$, which cause the losses are slightly higher than those in the 3-phase machine. Because the eddy current loss components are proportional to the product of frequency square and current amplitude, at high frequencies the reduction in current amplitude is outweighed by increase in frequency square. It should be noted that the total rotor iron loss is reduced in the proposed 9-phase winding configuration since the reduction of the eddy current loss components in rotor iron loss associated with 6^{th}, 12^{th}, 18^{th}, 24^{th}, 30^{th}, 42^{nd}, 48^{th}, 60^{th}, 66^{th}, 78^{th} $\cdots$ orders of harmonics is more than the loss increases in 36^{th}, 54^{th}, 72^{nd}, $\cdots$ orders.

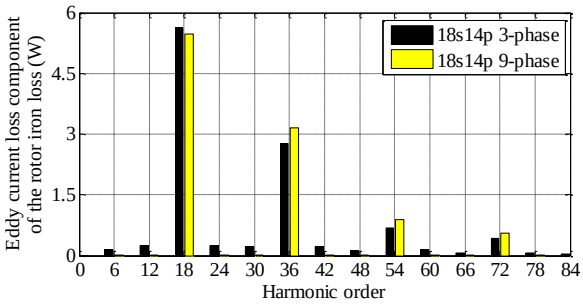

Fig. 8. Harmonic distributions of the eddy current loss component of the rotor iron loss.

Fig. 9 illustrates the efficiency difference map which is obtained by subtracting the efficiency map of the conventional 3-phase 18-slot 14-pole machine from that of the proposed 9-phase machine. It shows that by using the proposed 9-phase machine, the efficiency is improved at all the torque and speed operation conditions. The efficiency improvement at high torque and low speed region is more than that at low torque and high speed region. This is because the copper loss is dominant in the former region while the iron loss is dominant in the latter one. The iron loss reduction in the proposed 9-

phase machine is mainly obtained in the rotor core.

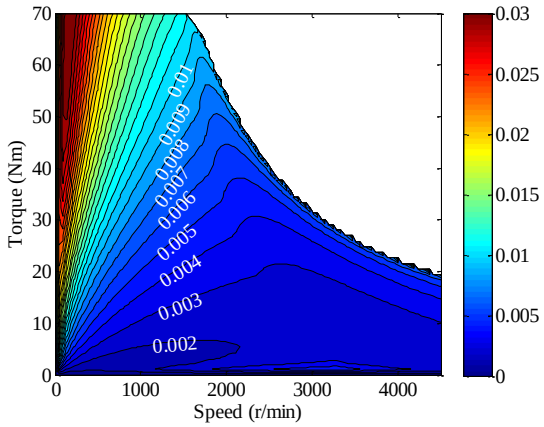

Fig. 9. Efficiency difference map between 9-phase and 3-phase 18-slot 14-pole machines.

The torque ripple is also reduced in the proposed 9-phase machine. At the peak torque and base speed, the torque ripple is reduced from 11.5% to 5.7%. This is due to the elimination of the 6th, 12th, 24th, 30th ⋯ order torque ripple harmonics, as shown in Fig. 10. This is because the torque harmonic components produced by the three 3-phase winding sets forms a balanced 3-phase system at these orders.

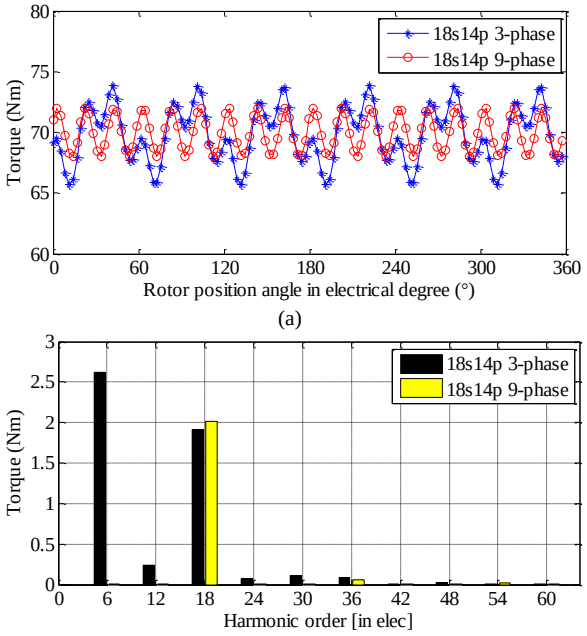

Fig. 10. Torque ripple comparison at 70Nm and 1350r/min. (a) Waveforms. (b) Spectra without DC components.

For example, the phase shift of the 6th order torque ripple harmonics between two neighboring 3-phase sets is 120° and thus they are cancelled out in a three 3-phase machine. This phenomenon can be understood by the fact that the 6th order torque ripple harmonic is produced by the interaction of the 5th and 7th order back-EMF harmonics with the fundamental current. The phase shifts of the 5th and 7th order back-EMF harmonics between two neighboring 3-phase sets are 5×20°=100° 7×20°=140°, respectively, while the current phase shift between two neighboring 3-phase sets is 20°. Consequently, the phase shift of the 6th order torque ripple harmonic contributed by the 5th order back-EMF harmonic is 100°+20°=120°, whilst that of the 7th order back-EMF harmonic is 140°-20°=120°.

From Fig. 10 (b), it can also be observed that the 18th order torque ripple harmonic remains in the 9-phase machine. This is because the phase shift of the18th order torque ripple harmonic between two neighboring 3-phase sets, resulting from the interaction of 17th and 19th back-EMF harmonics with the current is 17×20°+20°=360° or 19×20°-20°=360°. Thus, the torque ripple of each 3-phase set adds up. Moreover, the lowest order of cogging torque harmonic is also 18.

C. Performance Comparison with the Existing 3-Phase Machine

The performances of the proposed 9-phase 18-slot 14-pole machine are also compared with those of an existing air-cooled 3-phase 36-slot 6-pole IPM machine [26] whose schematic is shown in Fig. 11. The two machines are optimally designed against the same set of specifications for EV traction application with the same active volume and VA rating. However, the proposed machine exhibits a smaller total volume due to its shorter end-winding length. Moreover, stepped-skew technique has to be employed in the latter in order to reduce the torque ripple to an acceptable level.

The performance comparison of the proposed 9-phase 18-slot 14-pole IPM machine and the conventional 3-phase 36-slot 6-pole IPM machine is listed in Table VIII. It can be seen that the former can reach 93.5% rated efficiency which is only 0.2% lower than that of the latter. Due to more compact end-winding, the former has ~7% higher torque density than the latter. Meanwhile, the former uses 0.84kg bonded NdFeB while the latter needs 0.97kg sintered NdFeB. It should be noted that the efficiency of the proposed machine can be increased if it uses the sintered NdFeB magnets and/or has the same total volume as the latter.

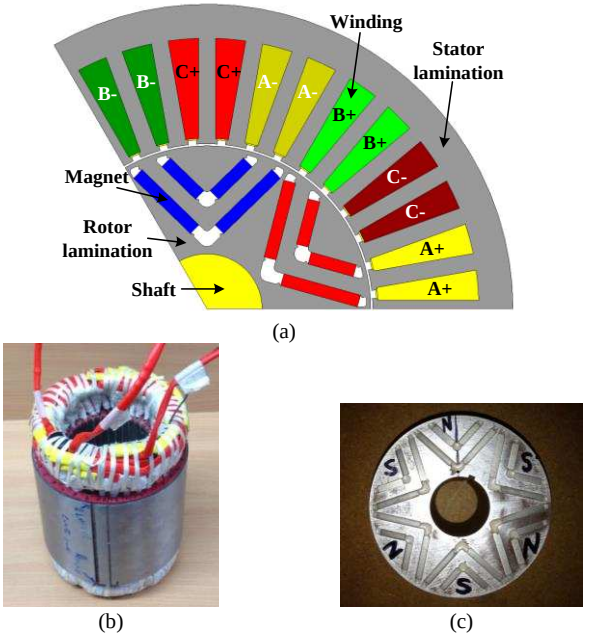

Fig. 11. Schematics of an existing 3-phase 36-slot 6-pole IPM machine. (a) Cross-section. (b) Stator stack. (c) Rotor stack.

TABLE VIII
PERFORMANCE COMPARISON BETWEEN THE CONVENTIONAL 3-PHASE 36-SLOT 6-POLE MACHINE AND PROPOSED 9-PHASE 18-SLOT 14-POLE MACHINE

Quantity	Unit	3-phase 36-slot 6-pole machine	9-phase 18-slot 14-pole machine
Outer diameter	mm	150	200
Active length	mm	118	66.4
End-winding Length	mm	147.9	63.7
Volume including end-winding	m^3	1.17×10^{-2}	1.09×10^{-2}
Torque density	Nm/m^3	6.0×10^3	6.4×10^3
Rated efficiency	%	93.7%	93.5%
PM type		Sintered NdFeB	Bonded NdFeB
PM usage	kg	0.97	0.84

Therefore, compared to the conventional IPM machine with sintered NdFeB material and distributed winding configuration, the proposed 9-phase 18-slot 14-pole IPM machine exhibits similar efficiency performance while it uses low grade and less rare-earth material, has shorter end-winding length, and less total volume. Stepped-skew is also avoided due to its low torque ripple, which is conducive to lower manufacturing cost.

VI. EXPERIMENTAL VALIDATION

An 18-slot 14-pole 9-phase IPM machine prototype is built to validate the foregoing FEA and MMF harmonics cancellation effects. The machine prototype and experimental set-up is illustrated in Fig. 11. Since a 9-phase inverter is not readily available, the tests were performed in generation mode of operation. Given that the d-axis current is always negative in both motoring and generation and the machine flux linkage map is almost symmetrical with respect to q-axis current, the test results in generation mode should also be representative of motoring operations, albeit the loss due to high frequency Pulse Width Modulation (PWM) will not be present.

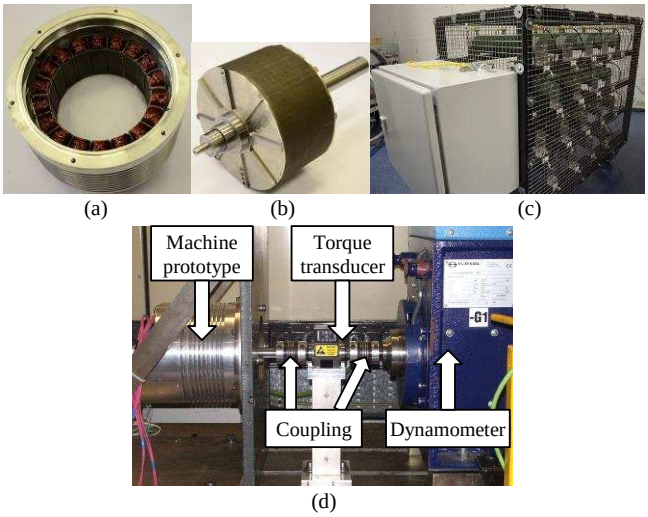

Fig. 11. Machine prototype and experimental setup. (a) Stator. (b) Rotor. (c) Resistive load. (d) Experimental setup.

The prototype machine is connected to a dynamometer via a high precision in-line torque transducer, and it is driven by the dynamometer during the tests.

A. No-Load Test

First, the machine prototype is driven without load to validate the back-EMF predicted by FEA. The FE-predicted and measured phase back-EMFs are compared in Fig. 12. The fundamental back-EMF of the machine prototype is 1.7% higher than the FEA result under the same speed and temperature conditions. This is because the rotor stack length in the prototype machine is 6mm longer than that of the stator in order to compensate potential flux reduction due to 3-D effect which cannot be predicted by 2-D FEA.

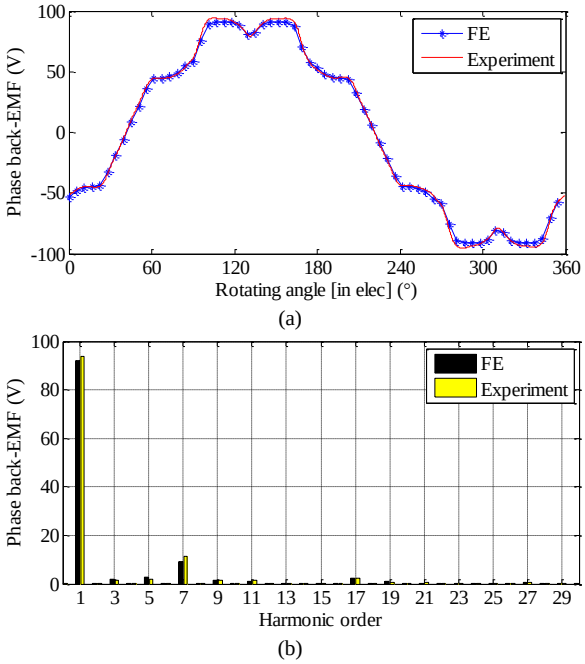

Fig. 12. Comparison of measured and FE predicted phase back-EMF at 1350r/min and 25°C. (a) Waveforms. (b) Spectra.

The no-load loss is measured by the torque transducer shown in Fig. 11 (d) at various speeds, and the comparison between the measured no-load loss and the FE-predicted iron loss is shown in Fig. 13. It can be observed that the measured no-load loss is much higher than the FE predicted no-load iron loss. This is due to the fact that the measured no-load loss includes both the iron loss and the mechanical loss (friction and windage) and in addition, the factors that may affect iron loss during manufacturing such as mechanical and thermal stress are not accounted in the FE prediction. Therefore, a build factor (1.3 for this machine) is introduced to calibrate the no-load loss model. It can be seen from Fig. 13 that with a build factor of 1.3, the FE-predicted iron loss agrees well with the measurements.

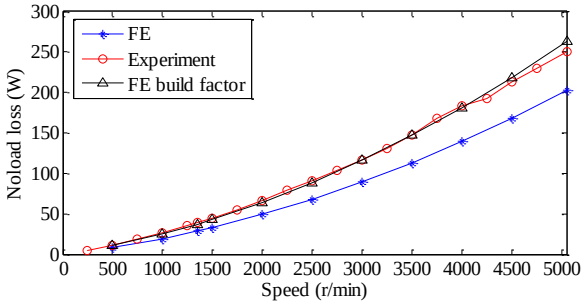

Fig. 13. Measured and predicted no-load loss variation with speed.

B. Load Test in Generator Mode

The machine prototype is driven by the dynamometer and operates in the generator mode with resistive loads for the experimental validation of electromagnetic behaviors under load conditions. The experimental setup is shown in Fig. 11 (d) and the resistive load bank is shown in Fig. 11 (c). The voltage and current waveforms are measured using high precision voltage and current transducers and the data are captured with high resolution oscilloscopes.

On-load tests are performed against four load conditions with the load resistance at 6.875Ω, 10Ω, 22Ω and 32Ω, respectively. For each load condition, the speed varies from 250r/min to the speed at which the maximum power is reached. The measured and FE-predicted voltage and current waveforms as well as the average torque are compared. Good agreements are observed for all four operating points between the predictions and measurements.

By way of example, Fig. 14 compares the measured and FE-predicted phase voltage and phase current, at 3250r/min with 22Ω load. The output power of the machine at this load condition is 4.5kW.

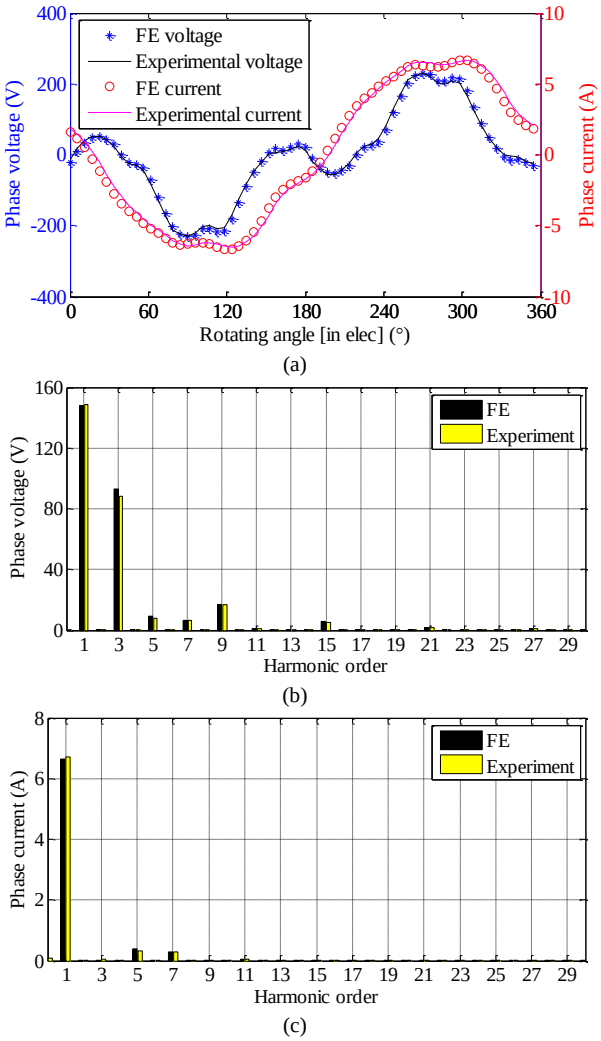

Fig. 14. Comparison of measured and FE-predicted phase voltage and current at 3250r/min with 22Ohm load. (a) Waveforms. (b) Phase voltage FFT spectra. (c) Phase current FFT spectra.

It can be seen that both the FE-predicted phase voltage and phase current agree well with the experimental results. The errors in fundamental phase voltage and current are 0.1% and 0.8%, respectively, which might result from the combined effect of modeling and measurement errors. It should be noted that the current and voltage waveforms in Fig. 14 (a) contains high order harmonics which are caused by the harmonics in the back-EMF since the machine operates at the generator mode. These harmonics in the phase current and voltage will result in additional copper loss, iron loss and torque ripple. However, the current waveform will be close to sinusoid in the motoring operation under inverter feedback control.

The comparison of the predicted and measured torque is shown in Fig. 15 under the same condition as described for Fig. 14. Due to bandwidth limit of the torque transducer, the instantaneous torque waveform at 2.3kHz cannot be captured, and thereby only the mean torque value of the experimental result is shown in Fig. 15. The measured mean torque is 3.7% higher than the FE prediction. This is mainly due to the fact that the mechanical loss and iron loss which contributes to the input torque in generator mode is not accounted in the FE-predicted torque.

Therefore, the electromagnetic behaviors of the proposed machine are also validated under load conditions.

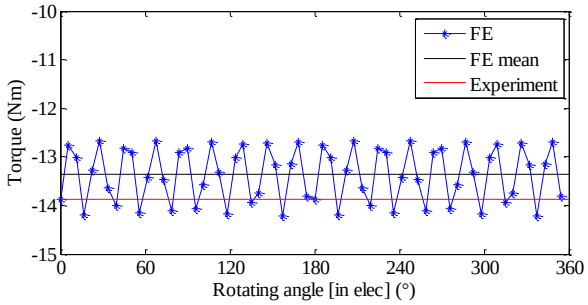

Fig. 15. Comparison of the measured and FE-predicted torque at 3250r/min with 22Ω load.

C. Discussion

To demonstrate the effect of the space harmonic cancellation which results with the proposed technique, the on-load tests with only one 3-phase (ABC) and with two 3-phases, ABC and DEF are also performed under the same load condition as the three 3-phase operation in Fig. 14 for each 3-phase set. The input and output powers of each test are measured and the resultant total loss is obtained. With measured winding temperature in each test, the copper loss can be accurately quantified and the sum of the iron loss and mechanical loss is determined by subtracting the copper loss from the total loss. Table IX summarizes the test results obtained from one 3-phase, two 3-phase and three 3-phase operations. It can be observed that the ratio of the sum of the iron loss and mechanical loss to the input power are 7.7%, 4.7% and 2.9% for one 3-phase, two 3-phase and three 3-phase operations, respectively. Given that the mechanical loss in each operation should be approximately equal, the increases in the measured mechanical and iron losses in the one 3-phase and two 3-phase operations can only be explained by the

presence of more space harmonics which have otherwise been cancelled by the proposed technique in the three 3-phase operation. This observation is indeed supported by FE-predicted iron losses, also given in Table IX, for the three operations. It has been shown from the FEA that the presence of the more undesirable space harmonics in the one 3-phase and two 3-phase operations gives rise to more significant distortion in flux density waveforms in the stator and rotor cores, and hence increase in iron loss. This indicates the effectiveness of the MMF harmonics cancellation effect in the proposed machine.

TABLE IX
POWER AND LOSSES

Item	ABC on	ABC,DEF on	ABC,DEF,GHI on
Measured mean torque (Nm)	5.6	10.1	13.9
Measured input power (W)	1915.8	3450.2	4722.4
Measured output power (W)	1736.2	3226.8	4498.6
Measured copper loss (W)	32.5	61.2	87.1
Measured Iron loss and mechanical loss(W)	147.1	162.2	136.8
Measured iron loss and mechanical loss ratio	7.7%	4.7%	2.9%
Measured efficiency (%)	90.6%	93.5%	95.3%
FE-predicted iron loss (W)	126.2	140.1	112.8
FE-predicted iron loss ratio	6.6%	4.1%	2.4%

To drive the proposed machine, a 9-phase inverter needs to be employed. This 9-phase inverter should be configured as three 3-phase inverters with standard modules, and each 3-phase inverter may be controlled based on conventional field oriented control technique. It should be noted that although the need for multiple 3-phase inverters for the proposed winding configuration might be seen as a disadvantage, the total inverter VA rating is the same as that of a 3-phase machine since the current rating of one 3-phase inverter is proportionally reduced. The use of three 3-phase inverters with low current rating spreads the inverter loss and is conducive to cooling and integration of the inverter into the machine. It also contributes to a degree of fault tolerance in that the machine can continue to operate even if one set of 3-phase winding/drive fails. This is valuable and significant for machines in EV traction application where the safety requirement of the powertrain system is relatively high. Moreover, the torque ripple can be dramatically reduced without skew techniques in that certain torque ripple harmonics can be completely cancelled out. Therefore, it is worthwhile and advantageous to develop multiple 3-phase winding configurations for electrical machines in EV traction application.

VII. CONCLUSION

A methodology to reduce stator MMF harmonics in a 9-phase 18-slot 14-pole IPM machine with concentrated windings has been described. This is achieved by employing multiple 3-phase windings and selecting appropriate phase shifts in both space and time. The proposed winding configuration cancels out all the MMF sub-harmonics and some high order MMF harmonics. This technique is also applicable to other slot-pole combinations with concentrated windings except for those with slot number being equal to 1.5 times the pole number.

The reduction in MMF harmonics leads to a number of benefits. Firstly it reduces both stator and rotor iron losses, particularly at high speeds, and hence, prevents excessive rotor temperature. It also significantly reduces torque ripple since the torque ripples associated with a specific set of harmonics are cancelled in a multiple 3-phase machine. Moreover, it also improves reluctance torque capability of IPM machines with concentrated windings because the MMF sub-harmonics which lead to localized saturation in the rotor and reduction in rotor saliency have been eliminated.

Compared to the MMF harmonic reduction techniques in literature, the proposed machine topology in this paper retains the advantages of the concentrated windings and exhibits a high winding factor, low torque ripple, low manufacture cost, high torque density and the high efficiency over wide torque and speed ranges.

REFERENCES

[1] C. C. Chan, "The State of the Art of Electric, Hybrid, and Fuel Cell Vehicles," Proceedings of the IEEE, vol. 95, pp. 704-718, 2007.

[2] M. W. Brainard, "Synchronous Machines with Rotating Permanent-Magnet Fields; Part I. Characteristics and Mechanical Construction [includes discussion]," Power Apparatus and Systems, Part III. Transactions of the American Institute of Electrical Engineers, vol. 71, 1952.

[3] J. Wang, X. Yuan, and K. Atallah, "Design Optimization of a Surface-Mounted Permanent-Magnet Motor With Concentrated Windings for Electric Vehicle Applications," Vehicular Technology, IEEE Transactions on, vol. 62, pp. 1053-1064, 2013.

[4] I. Boldea, L. N. Tutelea, L. Parsa, and D. Dorrell, "Automotive Electric Propulsion Systems With Reduced or No Permanent Magnets: An Overview," Industrial Electronics, IEEE Transactions on, vol. 61, pp. 5696-5711, 2014.

[5] X. Chen, J. Wang, P. Lazari, and L. Chen, "Permanent Magnet Assisted Synchronous Reluctance Machine with fractional-slot winding configurations," in Electric Machines & Drives Conference (IEMDC), 2013 IEEE International, 2013, pp. 374-381.

[6] P. B. Reddy, A. M. El-Refaie, H. Kum-Kang, J. K. Tangudu, and T. M. Jahns, "Comparison of Interior and Surface PM Machines Equipped With Fractional-Slot Concentrated Windings for Hybrid Traction Applications," Energy Conversion, IEEE Transactions on, vol. 27, pp. 593-602, 2012.

[7] R. Dutta and M. F. Rahman, "Design and Analysis of an Interior Permanent Magnet (IPM) Machine With Very Wide Constant Power Operation Range," Energy Conversion, IEEE Transactions on, vol. 23, pp. 25-33, 2008.

[8] G. Pellegrino, A. Vagati, P. Guglielmi, and B. Boazzo, "Performance Comparison Between Surface-Mounted and Interior PM Motor Drives for Electric Vehicle Application," Industrial Electronics, IEEE Transactions on, vol. 59, pp. 803-811, 2012.

[9] H. Cai, B. Guan, and L. Xu, "Low-Cost Ferrite PM-Assisted Synchronous Reluctance Machine for Electric Vehicles," Industrial Electronics, IEEE Transactions on, vol. 61, pp. 5741-5748, 2014.

[10] S. Morimoto, M. Sanada, and Y. Takeda, "Performance of PM-assisted synchronous reluctance motor for high-efficiency and wide constant-power operation," Industry Applications, IEEE Transactions on, vol. 37, pp. 1234-1240, 2001.

[11] R. Dutta, L. Chong, and M. F. Rahman, "Design and Experimental Verification of an 18-Slot/14-pole Fractional-Slot Concentrated Winding Interior Permanent Magnet Machine," Energy Conversion, IEEE Transactions on, vol. 28, pp. 181-190, 2013.

[12] A. M. El-Refaie, "Fractional-Slot Concentrated-Windings Synchronous Permanent Magnet Machines: Opportunities and Challenges," Industrial Electronics, IEEE Transactions on, vol. 57, pp. 107-121, 2010.
[13] N. Bianchi and E. Fornasiero, "Impact of MMF Space Harmonic on Rotor Losses in Fractional-Slot Permanent-Magnet Machines," Energy Conversion, IEEE Transactions on, vol. 24, pp. 323-328, 2009.
[14] J. Wang, K. Atallah, R. Chin, W. M. Arshad, and H. Lendenmann, "Rotor Eddy-Current Loss in Permanent-Magnet Brushless AC Machines," Magnetics, IEEE Transactions on, vol. 46, pp. 2701-2707, 2010.
[15] P. B. Reddy, H. Kum-Kang, and A. M. El-Refaie, "Generalized Approach of Stator Shifting in Interior Permanent-Magnet Machines Equipped With Fractional-Slot Concentrated Windings," Industrial Electronics, IEEE Transactions on, vol. 61, pp. 5035-5046, 2014.
[16] G. Dajaku, "Elektrische machine," Germany Patent DE 102 008 057 349, Jul. 15, 2010.
[17] G. Dajaku and D. Gerling, "A Novel 24-Slots/10-Poles Winding Topology for Electric Machines," in Electric Machines & Drives Conference (IEMDC), 2011 IEEE International, 2011, pp. 65-70.
[18] G. Dajaku and D. Gerling, "A novel tooth concentrated winding with low space harmonic contents," in Electric Machines & Drives Conference (IEMDC), 2013 IEEE International, 2013, pp. 755-760.
[19] G. Dajaku, W. Xie, and D. Gerling, "Reduction of Low Space Harmonics for the Fractional Slot Concentrated Windings Using a Novel Stator Design," Magnetics, IEEE Transactions on, vol. 50, pp. 1-12, 2014.
[20] J. Wang, V. I. Patel, and W. Wang, "Fractional-Slot Permanent Magnet Brushless Machines with Low Space Harmonic Contents," Magnetics, IEEE Transactions on, vol. 50, pp. 1-9, 2014.
[21] V. I. Patel, J. Wang, W. Wang, and X. Chen, "Six-Phase Fractional-Slot-per-Pole-per-Phase Permanent-Magnet Machines With Low Space Harmonics for Electric Vehicle Application," Industry Applications, IEEE Transactions on, vol. 50, pp. 2554-2563, 2014.
[22] N. Bianchi, S. Bolognani, Pre, x, and M. D., "Magnetic Loading of Fractional-Slot Three-Phase PM Motors With Nonoverlapped Coils," Industry Applications, IEEE Transactions on, vol. 44, pp. 1513-1521, 2008.
[23] X. Chen, J. Wang, and V. I. Patel, "A Generic Approach to Reduction of Magnetomotive Force Harmonics in Permanent-Magnet Machines With Concentrated Multiple Three-Phase Windings," Magnetics, IEEE Transactions on, vol. 50, pp. 1-4, 2014.
[24] P. Lazari, J. Wang, and L. Chen, "A Computationally Efficient Design Technique for Electric-Vehicle Traction Machines," Industry Applications, IEEE Transactions on, vol. 50, pp. 3203-3213, 2014.
[25] L. Chen, J. Wang, P. Lombard, P. Lazari, and V. Leconte, "Design optimisation of permanent magnet assisted synchronous reluctance machines for electric vehicle applications," in Electrical Machines (ICEM), 2012 XXth International Conference on, 2012, pp. 2647-2653.
[26] X. Chen, J. Wang, B. Sen, P. Lazari, and T. Sun, "A High-Fidelity and Computationally Efficient Model for Interior Permanent-Magnet Machines Considering the Magnetic Saturation, Spatial Harmonics, and Iron Loss Effect," Industrial Electronics, IEEE Transactions on, vol. 62, pp. 4044-4055, 2015.

Xiao Chen (S'13-M'16) born in Taian, China, in 1988, received B.Eng. degree in electrical engineering from Harbin Institute of Technology at Weihai, Weihai, China, in 2009, M.Eng. degree in electrical engineering from Harbin Institute of Technology, Harbin, China, in 2011, and Ph.D degree in electrical engineering from The University of Sheffield, Sheffield, UK, in 2015. He is currently a Research Associate in the Department of Electronic and Electrical Engineering, The University of Sheffield, UK. His current research interests include the modeling, design and analysis of permanent-magnet synchronous machines for traction applications.

Jiabin Wang (S'94–A'96–M'01–SM'03) received the B.Eng. and M.Eng. degrees from Jiangsu University of Science and Technology, Zhenjiang, China, in 1982 and 1986, respectively, and the Ph.D. degree from the University of East London, London, U.K., in 1996, all in electrical and electronic engineering.

Currently, he is a Professor in Electrical Engineering at the University of Sheffield, Sheffield, U.K. From 1986 to 1991, he was with the Department of Electrical Engineering at Jiangsu University of Science and Technology, where he was appointed a Lecturer in 1987 and an Associated Professor in 1990. He was a Postdoctoral Research Associate at the University of Sheffield, Sheffield, U.K., from 1996 to 1997, and a Senior Lecturer at the University of East London from 1998 to 2001. His research interests range from motion control and electromechanical energy conversion to electric drives for applications in automotive, renewable energy, household appliances and aerospace sectors.

He is a fellow of the IET and a senior member of IEEE.

Vipulkumar I. Patel (S'13-M'15) was born in Gujarat, India, in 1982. He received the B.E. degree in electrical engineering from Gujarat University, Ahmedabad, India, in 2003, the M.Tech. degree in power electronics, electrical machines, and drives from the Indian Institute of Technology Delhi, New Delhi, India, in 2005, and the Ph.D. degree in electronic and electrical engineering from The University of Sheffield, Sheffield, U.K., in 2014.

He is currently a Senior Customer Support Engineer with Mitsubishi Hitachi Power Systems Europe Ltd. From 2014 to 2015, he was a Research Assistant in electronic and electrical engineering with The University of Sheffield. From 2005 to 2010, he was a Lead Engineer with the GE India Technology Centre, Bangalore, India. His research interests include design and analysis of permanent-magnet machines for various industrial applications.

Dr. Patel was a recipient of the IEEE Power Electronics, Drives and Energy Systems '96 Award for the Best Performance in the Area of Power Electronics, Electrical Machines, and Drives in 2005.

Panagiotis Lazari (S'13) was born in Limassol, Cyprus, in 1986. He received the B.Eng. degree in 2010 from the Department of Electronic and Electrical Engineering, The University of Sheffield, UK, where he is currently working towards the Ph.D. degree on the development of traction machines for EV applications.